Field-induced magnetic transitions in the highly anisotropic ferrimagnet $ErFe_5Al_7$ studied by high-field x-ray magnetic dichroism

Sh. Yamamoto,[1,*] D. I. Gorbunov,[1] O. Prokhnenko,[2] E. Weschke,[2] A. Miyata,[1] I. F. Diaz-Ortega,[3,4] C. Strohm,[5] F. Duc,[6] M. S. Henriques,[7] A. Gazizulina,[2] M. Uhlarz,[1] O. Mathon,[8] A. V. Andreev,[7] H. Nojiri,[4] and J. Wosnitza[1,9]

[1]*Hochfeld-Magnetlabor Dresden (HLD-EMFL) and Würzburg-Dresden Cluster of Excellence ct.qmat, Helmholtz-Zentrum Dresden-Rossendorf, 01328 Dresden, Germany*

[2]*Helmholtz-Zentrum Berlin für Materialien und Energie, BESSY II, 12489 Berlin, Germany*

[3]*Área de Química Inorgánica-CIESOL, Universidad de Almería, Ctra. Sacramento s/n, 04120, Almería, Spain*

[4]*Institute for Materials Research, Tohoku University, Sendai 980-8577, Japan*

[5]*Deutsches Elektronen Synchrotron, Notkestrasse 85, 22607 Hamburg, Germany*

[6]*CNRS, Laboratoire National des Champs Magnétiques Intenses, Université Grenoble Alpes, Université Toulouse 3, INSA Toulouse, EMFL, 31400 Toulouse, France*

[7]*Institute of Physics of the Czech Academy of Sciences, 18200 Prague, Czechia*

[8]*European Synchrotron Radiation Facility, Boîte Postale 220, 38043 Grenoble, France*

[9]*Institut für Festkörper- und Materialphysik, TU Dresden, 01062 Dresden, Germany*

(Received 23 November 2023; revised 15 January 2024; accepted 9 February 2024; published 5 March 2024)

We present a comprehensive study of the magnetic properties of the strongly anisotropic ferrimagnet $ErFe_5Al_7$ in pulsed magnetic fields up to 30 T applied along the hard magnetization axis within the basal plane of the tetragonal lattice around the compensation temperature (T_{comp}). Macroscopic measurements showed two anomalies at about 8 T and 25 T in a small temperature range around T_{comp}. High-field x-ray magnetic circular dichroism (XMCD) data at the Er M_5- and the Fe L_3-edge resonances provide insight into the element-selective magnetization processes, revealing a coherent rotation of Er $4f$ and Fe $3d$ moments, with stepwise jumps including an unexpected one from an easy to a hard magnetization axis. XMCD at the Er L_3-edge resonance elucidates the role of Er $5d$ electrons in coupling the Er $4f$ and the Fe $3d$ moments. Finally, an in-plane anisotropy constant was evaluated from a simulation of the magnetization process at temperatures well below T_{comp} using a two-sublattice model.

DOI: 10.1103/PhysRevB.109.094404

I. INTRODUCTION

Rare-earth (R) transition-metal (T) intermetallic compounds are a prominent class of materials with applications as permanent magnet as well as in magneto-optical and magnetostrictive devices, originating from an interplay between large magnetic anisotropies of the R sublattice and strong exchange interactions of the T sublattice [1]. These magnetic properties are established by three exchange interactions between T–T, R–T, and R–R atoms. The strongest (T–T) exchange leads to high ordering temperatures (T_C) and large spontaneous magnetizations. The next-largest (R–T) exchange is responsible for transferring large magnetic anisotropy of the R sublattice to the T counterpart. The R–T exchange interaction also transfers the exchange interactions of the T sublattice to R that keep the R moments ordered up to T_C, a much higher temperature than if there was no T sublattice. The weakest (R–R) interaction is usually disregarded [2]. In R-T intermetallic compounds with heavy R elements, the R–T intersublattice exchange interaction is antiferromagnetic, which is mediated by the intra- and interatomic exchange $R(4f)$–$R(5d)$–$T(3d)$ interactions [3].

The antiparallel spin alignments in R–T ferrimagnets are destabilized by large applied magnetic fields of tens of teslas [4–9]. The magnetization in such anisotropic R–T ferrimagnets exhibits a sequence of phase transitions, which are not seen for isotropic ferrimagnets [10]. The complex and diverse magnetization processes are connected with large field-induced noncollinearity. A detailed determination of the microscopic magnetization processes at some high magnetic fields is crucial for modeling the fundamental magnetic properties. However, conventional bulk magnetization experiments only detect total magnetic moments [11], and it is challenging to study experimentally the microscopic nature of the field-induced magnetic transitions of R-T intermetallic systems with two magnetic species in such high magnetic fields.

RFe_5Al_7 with tetragonal crystal structure (space group $I4/mmm$) exhibits strongly anisotropic ferrimagnetic properties with easy-plane (R = Tb, Dy, Ho, and Er) or easy-axis (R = Tm) anisotropy at low temperatures. The R, some Fe, and some Al atoms occupy the $2a$, $8f$, and $8i$ sites, respectively. The rest of the Fe and Al atoms share the $8j$ site [12]. The balance between exchange and anisotropy interactions is modified at high magnetic fields, which results in

*s.yamamoto@hzdr.de

field-induced magnetic transitions with a noticeable spin-lattice coupling under magnetic fields applied along the easy magnetization axis [12].

Indeed, our high-field x-ray magnetic circular dichroism (XMCD) experiments of RFe$_5$Al$_7$ (R = Tb, Ho, and Tm) have recently evidenced that the field-induced transitions correspond to a simultaneous step-wise rotation of the R and Fe moments [13–15]. At the magnetic transition, in RFe$_5$Al$_7$ with easy-plane anisotropy (R = Tb and Ho), the magnetic moments rotate within the basal plane of the tetragonal lattice from one easy magnetization axis to another one by 90 degrees, while in TmFe$_5$Al$_7$ with easy-axis anisotropy, the magnetic moments almost flip from a collinear ferrimagnetic order to a magnetic state close to the forced ferromagnetic state. Our element-specific magnetization processes were successfully described by a two-sublattice model with a R-T intersublattice exchange coupling, magnetocrystalline anisotropy, and Zeeman interactions [13–15].

ErFe$_5$Al$_7$ is exceptional in this RFe$_5$Al$_7$ family of compounds with heavy R elements, since it shows field-induced transitions under magnetic fields applied along the hard magnetization axis [110] as well as along the easy axis [100] within the basal plane of the tetragonal lattice. ErFe$_5$Al$_7$ orders with a collinear ferrimagnetic structure [16] at the Curie temperature $T_C = 201$ K, and has a compensation point of $T_{comp} = 33$ K [17], where the magnitudes of the Er and Fe magnetic moments are equal.

Preceding studies theoretically predict that in R-T intermetallic compounds, when a magnetic field is applied along a hard magnetization axis in the basal plane, the magnetic moments jump between easy magnetization axes like those under magnetic fields applied along an easy-axis direction [18]. However, the moment-rotation scheme in magnetic fields applied along the hard magnetization axis is not well understood experimentally in anisotropic R-T intermetallic compounds at this time. ErFe$_5$Al$_7$ is a good model system to investigate how each sublattice moment responds to the magnetic field applied along the hard magnetization axis within the basal plane of the tetragonal lattice. In some R-T systems, a so-called first-order magnetization process (FOMP) occurs when magnetic fields are applied along a hard axis [19,20]. The FOMP originates from the presence of two inequivalent minima in the magnetic-anisotropy energy and reflects the rotation of magnetization between two corresponding inequivalent directions. Such FOMPs should be distinguished from the field-induced transitions observed for field applied along the hard [110] axis of ErFe$_5$Al$_7$ with easy-plane anisotropy.

In this study, we present magnetization, magnetostriction, and x-ray magnetic dichroism data of an ErFe$_5$Al$_7$ single crystal under pulsed magnetic fields applied along the basal-plane hard axis [110], focusing on the microscopic nature of the two field-induced magnetic transitions observed around T_{comp}. In contrast to previous assumptions, we found that one of the field-induced transitions accompanied by strong magnetoelastic couplings originates in a magnetic-moment rotation from the easy to hard magnetization axis. The other field-induced transition corresponds to a jump from the easy magnetization direction to the forced ferromagnetic state. A two-sublattice model successfully simulates the magnetization process at

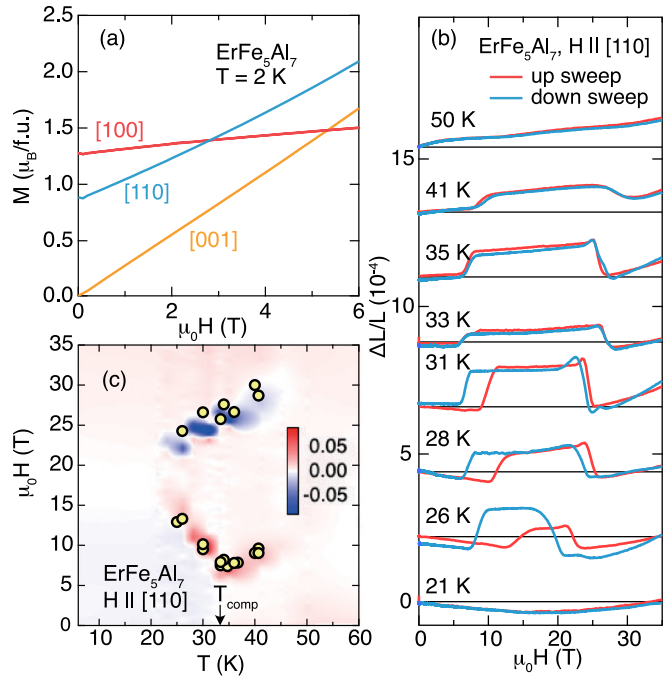

FIG. 1. (a) Magnetization as function of magnetic field applied along the [100], [110], and [001] axis. Data are from down field sweep. (b) Field dependence of relative length change $\Delta L/L$ in magnetic fields applied along the hard axis [110] within the basal plane of the tetragonal lattice of ErFe$_5$Al$_7$. Red and blue lines are data from up and down field sweeps. (c) Color-coded plot of $d(\Delta L/L)/dH$ of the up-sweep data with the compensation temperature T_{comp}. Symbols exhibit anomalies in the field-dependent magnetization data.

10 K, which enables us to extract the in-plane anisotropy constant.

II. EXPERIMENTAL

Bulk magnetization and magnetostriction measurements were measured in magnetic fields applied along the [110] axis using a coaxial pickup-coil system [18] and an optical fiber Bragg-grating (FBG) technique [21], respectively. The Er $M_{4,5}$- and Fe $L_{2,3}$-edge x-ray absorption spectroscopy (XAS) and XMCD measurements were conducted in the total-electron yield (TEY) mode at the UE46-PGM1 undulator beamline of BESSY II. The Er L_3-edge XAS and XMCD experiments were carried out in the transmission mode at the energy dispersive x-ray absorption spectroscopy beamline ID24 at ESRF [22,23]. Both XMCD measurements at BESSY II and ESRF were conducted using pulsed magnetic fields up to 30 T applied along the [110] axis. Details of the synchrotron experimental methods are described in Appendix A.

III. MAGNETIC PHASE DIAGRAM

Figure 1(a) shows magnetization data (M) under magnetic fields applied along the principal crystallographic axes. There is a spontaneous magnetization for magnetic fields applied along the [100] and [110] axis, while M starts at zero for field applied along the [001] direction. Therefore, the magnetic

moments lie in the basal plane. Considerable anisotropy is also observed within the basal plane between the [100] and [110] axes. The [110] axis is the hard direction within the basal plane of the tetragonal lattice. The ratio of the spontaneous magnetizations for the [110] and [100] directions, $M_s^{[110]}/M_s^{[100]}$, is equal to cos(45°), which signals that in a remanent state, the moment lies along the easy [100] axis. The basal-plane anisotropy weakens with increasing temperature and disappears around 140 K [17].

Figure 1(b) shows the longitudinal relative length change $\Delta L/L$ measured by the optical FBG technique [21] in magnetic fields applied along the [110] axis at the selected temperatures. At 26 K $< T <$ 41 K, around $T_{\rm comp}$, hysteretic stepwise anomalies exhibiting lattice expansions and contractions of $\sim$1–2 $\times$ 10^{-4} are observed below 30 T. Typically, $\Delta L/L$ steps with such magnitude are observed at field-induced magnetic transitions connected with magnetic-moment rotations in R-T intermetallic systems [15,24]. At lower temperatures, between 41 and 26 K, the hysteresis becomes more evident at the field-induced transitions, which implies that the nature of the transitions is first order.

The phase diagram derived from the field derivative of $\Delta L/L$ is shown in Fig. 1(c). The anomalies observed in $\Delta L/L$ agree with those seen in bulk magnetization data [symbols in Fig. 1(c) and Figs. 3(b) and 3(c) below]. The temperature dependence of the lower critical field [$d(\Delta L/L)/dH > 0$], H_{c1}, has a minimum at the compensation point, while the higher critical field [$d(\Delta L/L)/dH < 0$], H_{c2}, shows a monotonous decrease with decreasing temperature. $H_{c1}(T)$ follows the temperature dependence of the total magnetization [17].

IV. ZERO-FIELD REMANENT PROPERTIES

Since field-induced transitions, observed for magnetic fields applied along the hard [110] direction of $ErFe_5Al_7$, should reflect the variations of the individual magnetic moments, we use an element- and shell-selective experimental technique to reveal the microscopic nature of these transitions. Figures 2(a) and 2(b) show the Er $M_{4,5}$- and the Fe $L_{2,3}$-edge XAS and XMCD spectra in remanence after applying a 30-T pulsed magnetic field ($\vec{H}_{\rm pre}$) along the [110] axis at 10 K, respectively. The absorption spectrum for the right (μ^+) and left (μ^-) circular polarization in Figs. 2(a) and 2(b) was obtained by subtraction of a constant background of about 14% with respect to the XAS maximum for the μ^- polarization at the Er M_5 edge, and about 17% with respect to that for the μ^+ polarization at the Fe L_3 edge. These constant values were defined by the average of the pre-edge region of the Er M_5- and Fe L_3-edge resonance.

The Er spectral lineshapes are in good agreement with those observed for Er^{3+} [25]. The Fe $L_{2,3}$ line shape is essentially characteristic of metallic iron [26], with a small shoulder structure at the high-energy side. This shoulder is often observed in RFe_5Al_7, and may originate from some hybridization of the 8j-site Fe d and Al p states [14]. Likewise, this feature can be due to a small fraction of oxidized sample. Notably, the lineshape of the corresponding L-edge XMCD [Fig. 2(b)] does not include this feature, rendering the data of Fig. 2(c) as characteristic of the metallic sample fraction only. The XMCD amplitudes at the Er M_5- and the Fe L_3-edge

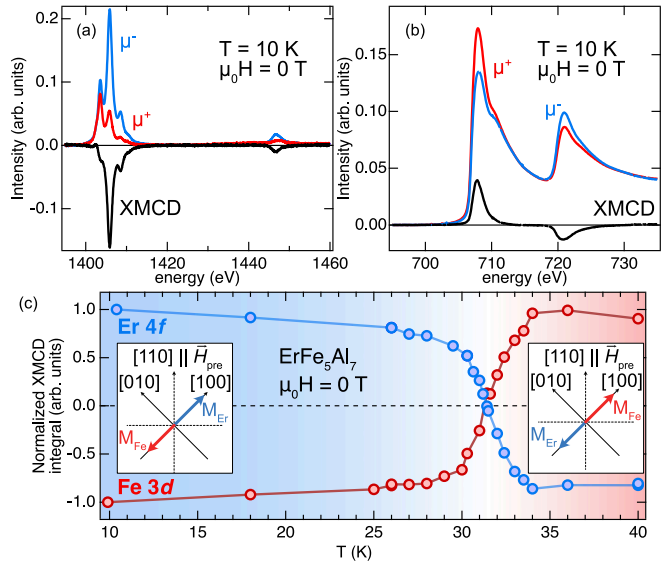

FIG. 2. XAS and XMCD spectra measured using circularly polarized light, μ^+ and μ^-, at the (a) Er M and (b) Fe L edges at 10 K under zero magnetic field. (c) Er M_5- (blue) and Fe L_3-edge (red) XMCD integrals as function of temperature under zero magnetic field. The signs of the integrals are reversed with respect to (a) and (b). The ferrimagnetic configuration in the red- and blue-colored area is shown schematically in the insets (see text for details). All the XMCD spectra were measured after applying a 30-T magnetic-field pulse along the [110] axis. $\vec{H}_{\rm pre}$ indicates the direction of the magnetic field pulse.

have the opposite sign, which evidences the antiferromagnetic coupling of the magnetic moments projected onto the [110] axis between the two sublattices. At 10 K, the projected Er 4f moments onto the [110] axis are parallel to $\vec{H}_{\rm pre}$ [110] and the projected Fe 3d counterparts are antiparallel to the [110] axis.

Figure 2(c) shows the temperature dependence of the XMCD integral at the Er M_5- and Fe L_3 edges normalized by those at 10 K. The sign of the normalized integrated intensity was reversed in Fig. 2(c) with respect to Figs. 2(a) and 2(b). Positive values of the reversed Er M_5- and Fe L_3-edge XMCD integrals correspond to the moment direction parallel to the field direction and negative ones to the moment direction antiparallel to $\vec{H}_{\rm pre}$. The antiparallel coupling of the magnetic moment projected on the [110] axis is clearly seen in the entire temperature range. Sign changes in the XMCD integrals at the two edges occur at 31.5 K. This reflects the nature of ferrimagnetic order in $ErFe_5Al_7$, i.e., the magnetic moment of the Fe 3d electrons is larger than that of the Er 4f electrons above 31.5 K and vice versa below 31.5 K. XMCD measurements using TEY detection are quite surface sensitive, with a probing depth of a few nanometers. This can explain the small difference of the compensation temperature observed by the macroscopic (33 K) and the soft XMCD measurements (31.5 K). In the following, the compensation temperature of 31.5 K observed in the soft XMCD is referred to as $T_{\rm comp}$.

The collinear magnetic structures below and above 31.5 K are shown at the schematic diagrams in Fig. 2(c). After applying $\vec{H}_{\rm pre}$ along the [110] axis, the sublattice moments

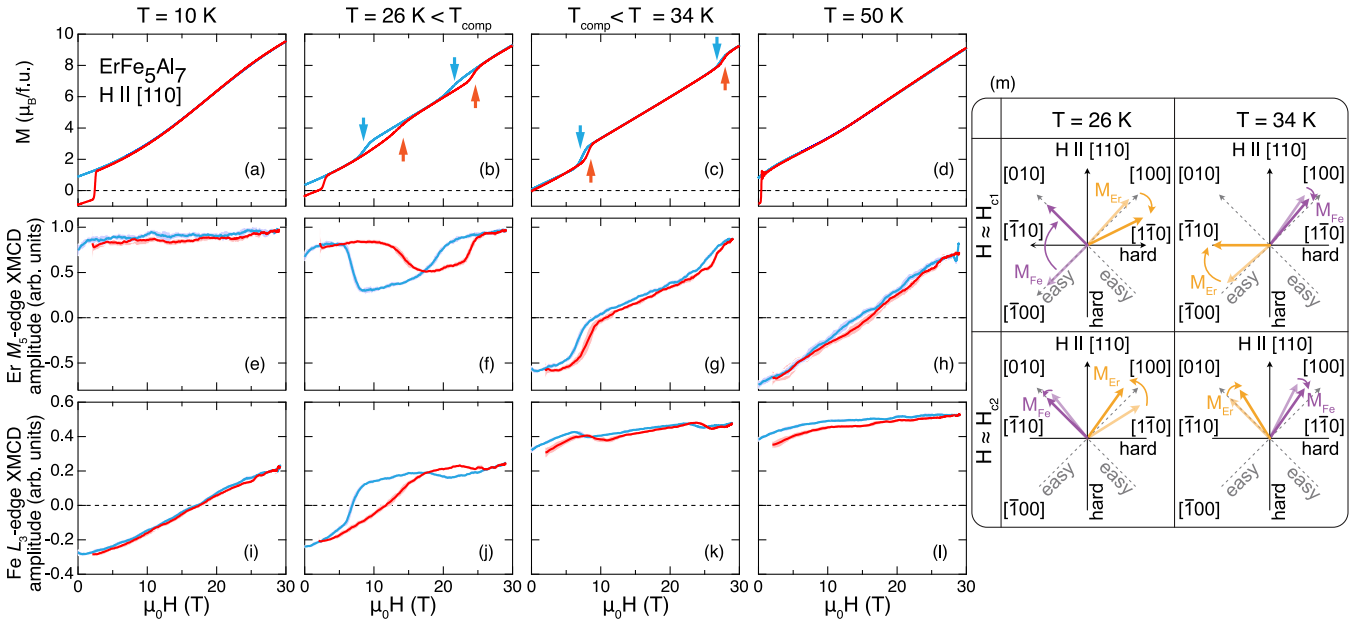

FIG. 3. (a)–(d) Bulk magnetization and (e)–(h) Er M_5-edge ($3d_{5/2} \rightarrow 4f$), and (i)–(l) Fe L_3-edge ($2p_{3/2} \rightarrow 3d$) XMCD amplitudes as functions of magnetic fields applied along the hard axis [110] within the basal plane of the tetragonal lattice at 10 K [(a), (e), and (i)], 26 K [(b), (f), and (j)], 34 K [(c), (g), and (k)], and 50 K [(d), (h), and (l)]. Red and blue lines are data from up and down field sweeps. The red and blue arrows in (b) and (c) denote anomalies observed during the up and down sweep of the field pulse, respectively. The sign of the Er M_5- and Fe L_3-edge XMCD amplitudes are reversed with respect to those in Figs. 2(a) and 2(b). The experimental errors in panels (e)–(l) are of the order of the thickness of the solid lines. (m) Configuration of the Er $4f$ moments (M_{Er}) and the Fe $3d$ moments (M_{Fe}) in the (001) plane deduced from the high-field soft XMCD results in panels (e)–(l) at 26 K and 34 K at the first (H_{c1}) and the second (H_{c2}) field-induced transitions. The hard and easy axes are shown by solid (black) and dashed (gray) lines, respectively.

lie in the axis along the easy axis [100]. The Fe L_3- and Er M_5-edge XMCD magnitudes decrease as the temperature approaches T_{comp}, and they reach zero at T_{comp}. There are three possibilities for this observation: (1) there are no ordered Er $4f$ and Fe $3d$ moments at T_{comp}, (2) Er $4f$ and Fe $3d$ ordered moments lie in the axis perpendicular to the [110] axis, and (3) there are equally populated domains (one domain is involved with the moments parallel to the [100] axis and the other one with those antiparallel to the [100] axis) within each magnetic sublattice.

This system orders ferrimagnetically below T_{C}, and there are no signatures in macroscopic measurements showing magnetic transition around T_{comp}, which excludes the possibility 1. The perpendicular orientation to the [110] axis is another hard axis within the basal plane. In addition, no spin-reorientation transition around T_{comp} is signaled by ultrasound and magnetization results [27]. These facts further exclude possibility 2.

A ferrimagnet is considered to be an antiferromagnet at a compensation temperature, where respective sublattices have exactly the same magnitude of their magnetic moments. In the remanent state after releasing the magnetic field, each sublattice moment does not know the direction of $\overrightarrow{H}_{\mathrm{pre}}$ at T_{comp}. In this case, half of the moments are parallel to the [100] axis, and the other half are antiparallel to the [100] axis. This gives two equally populated domains within each Er and Fe sublattice, and no net moments along the [110] axis. The ratio of the two domains gradually changes around T_{comp}, which leads to the observation of the gradual decrease of the XMCD magnitude around T_{comp}. Therefore, we conclude that scenario 3 is the reason for the behavior of the XMCD signals around T_{comp} in the remanent state. This scenario is further corroborated by the analysis of the field-dependent XMCD amplitudes near T_{comp}, assuming the existence of two domains (see Appendix B).

V. ROTATION SCHEME OF THE MAGNETIC MOMENTS

Next, we move to the soft XMCD results under magnetic fields, comparing them with the bulk magnetization. Figure 3 shows bulk magnetization as well as Er M_5- and Fe L_3-edge XMCD amplitudes as a function of magnetic fields up to 30 T applied along the [110] axis of $ErFe_5Al_7$ at the selected temperatures. The field-dependent XMCD amplitudes were measured at 1405.5 eV (Er M_5 edge) and 707.7 eV (Fe L_3 edge), corresponding to the respective XMCD maximum. The sign of the XMCD amplitudes is reversed with respect to those in Figs. 2(a) and 2(b).

At 10 K, well below T_{comp}, the bulk magnetization increases gradually without any anomalies except for the hysteresis related to domain-wall motion below ~2.5 T [Fig. 3(a)]. At 26 and 34 K, near T_{comp}, there are two magnetization jumps at H_{c1} and H_{c2} [Figs. 3(b) and 3(c)]. With further increasing temperature, at 50 K, far above T_{comp}, the bulk magnetization increases monotonously [Fig. 3(d)]. The forced-ferromagnetic state along the [110] axis is reached only above 60 T [27]. The field dependence of the Er M_5- and Fe L_3-edge XMCD amplitudes also display anomalies corresponding to those observed in the bulk magnetization at

26 K and 34 K [Figs. 3(f), 3(g), 3(j), and 3(k)]. Similar to the magnetostriction results, the bulk magnetization and soft XMCD data also show more pronounced hysteretic behavior at the field-induced transitions at 26 K as compared to 34 K. At 26 and 34 K, larger hystereses are observed at the field-induced transitions in the surface-sensitive soft XMCD results than in the bulk magnetization results. The field dependencies of the XMCD amplitude exhibit a very close correspondence to the bulk-sensitive of magnetostriction [Fig. 1(b)] and magnetization [Figs. 3(a)–3(d)] measurements, which is strong evidence that the field-dependent XMCD results represent the bulk properties of the material. Contrary, XMCD measurements on an uncleaved surface reveal saturation below 4 T and no field-induced hystereses (data not shown).

In the following, we discuss the magnetization processes of the Er $4f$ and Fe $3d$ electrons in magnetic fields, considering that the XMCD amplitudes reflect the projected component along the beam propagation direction parallel to the [110] axis. The variations of the XMCD amplitudes come from the coherent moment rotation either continuously or in a stepwise manner, rather than solely longitudinal variations of the magnetic moments, which will be discussed later. When a magnetic field is applied to the hard [110] axis, domains with collinear ferrimagnetic structure along the [100] and [010] axes coexist in equal populations. In the former domain, the Er and Fe magnetic moments point along the easy [100] and $[\bar{1}00]$ axis, respectively, below T_{comp} and vice versa above T_{comp}. The changes in the magnetic structures in magnetic fields from the collinear magnetic structure along the [010] axis can be equivalently discussed by reversing the orientation of the Er $4f$ and Fe $3d$ magnetic moments by 180 degrees around the [110] axis.

We start the discussion of our results at temperatures far away from T_{comp} (10 and 50 K). At 10 K, the projected Er $4f$ moments along the [110] axis stay almost constant up to 30 T [Fig. 3(e)]. On the other hand, the projected Fe $3d$ moments along the [110] axis continuously increase with a sign change at ∼18 T [Fig. 3(i)]. The Er $4f$ moment does not change the initial orientation [100], while the Fe $3d$ moment rotates from $[\bar{1}00]$ toward the other easy axis [010] up to 30 T with passing the hard axis $[\bar{1}10]$ at ∼18 T. The absence of an appreciable reduction of the Er $4f$ moments projected onto the [110] axis indicates that there is no detectable Er $4f$ moment rotation from [100] toward $[1\bar{1}0]$, which is likely due to a reduced Er-Fe intersublattice AFM coupling than that at higher temperatures close to T_{comp}. At 50 K, the relative orientation of the sublattice moments [Figs. 3(h) and 3(l)] is opposite with respect to that observed at 10 K. The Fe $3d$ moments slightly increase while the Er $4f$ moments rotate continuously up to 30 T.

Next, we turn to the results reflecting field-induced transitions around T_{comp} (26 K and 34 K). At 26 K, just below T_{comp}, the Fe L_3-edge XMCD amplitudes crosses zero and reaches the same XMCD magnitude at H_{c1} as that at 0 T [Fig. 3(j)] while the Er M_5-edge XMCD amplitudes strongly decrease [Fig. 3(f)]. This implies that the Fe $3d$ moments moves to the other easy axis [010], whereas the Er $4f$ moments rotate from the easy [100] axis toward the hard $[1\bar{1}0]$ direction [Fig. 3(m)]. With increasing magnetic fields from H_{c1} to H_{c2}, the Fe $3d$ moments rotate continuously toward the [110] axis, while the Er $4f$ moments rotate toward the [100] axis. At H_{c2}, the Er $4f$ moments pass the [100] axis, while the Fe $3d$ moments rotate slightly back to the [010] direction. Above H_{c2}, both the Er $4f$ and Fe $3d$ moments rotate toward the field direction along [110].

At 34 K, slightly above T_{comp}, the Er M_5-edge XMCD magnitude becomes zero at H_{c1} [Fig. 3(g)], while the Fe L_3-edge XMCD magnitude shows a weak reduction [Fig. 3(k)]. This means that at H_{c1}, the Er $4f$ moment jumps from the easy $[\bar{1}00]$ to the hard axis $[\bar{1}10]$ and the Fe $3d$ moment correspondingly shows slight rotation near [100] axis toward $[1\bar{1}0]$ [Fig. 3(m)]. With further increasing magnetic field, a second steeper increase of the Er $4f$-XMCD amplitudes appears at H_{c2} ∼ 27 T with again a weak reduction of the Fe L_3-edge XMCD counterpart. The Er XMCD magnitude just below H_{c2} is the same as that at zero field with opposite sign. This indicates that the Er $4f$ moment reaches the hard axis $[\bar{1}10]$ at H_{c1}, gradually rotates at magnetic fields between H_{c1} and H_{c2}, and the second transition occurs when the Er $4f$ moments reach the other easy axis [010]. The second jump in the Er M_5-edge XMCD amplitudes is smaller than the first one, which means that above H_{c2} the Er $4f$ moment still does not reach the [110] axis. Therefore, at 30 T, the system is still in a noncollinear magnetic state, which is consistent with the bulk magnetization results that shows no saturation at 30 T [Fig. 3(c)].

It is worth noting that in R-T intermetallic systems with collinear ferrimagnetic structure, when a magnetic field is applied along the easy magnetization axis, the magnetic moments rotate from one easy to another easy axis at field-induced magnetic transitions [13,15,18]. However, we observed that the Er $4f$ magnetic moments rotate from the easy to the hard axis at H_{c1} in $ErFe_5Al_7$ even at an intermediate magnetic field below saturation when a magnetic field is applied along the in-plane hard axis. This unusual behavior at the first magnetic transition was also seen in the field-dependent Er M_5-edge XMCD amplitudes at 40 K (not shown).

Our element-specific XMCD results clarify the moment-rotation scheme within the basal plane up to 30 T and 50 K. Comparing the results at 10 and 50 K, far away from T_{comp}, the response of the sublattice magnetization to the magnetic field reflects some symmetry between the Er and Fe moments. At 10 K, the Er $4f$ moments stay along the easy [100] axis, while the Fe $3d$ moments continuously rotate from the easy axis $[\bar{1}00]$ to [010]. At 50 K, on the other hand, the Fe $3d$ moments stay along the [100] axis, while the Er $4f$ moments coherently rotate from $[\bar{1}00]$ to [010].

This indicates that the Er-Fe antiferromagnetic exchange interaction is not dominant at temperatures away from T_{comp}. If this intersublattice interaction plays a role, the magnetic moment with the larger magnitude should move away from the easy [100] axis to keep the initial antiparallel configuration for as long as possible. On the other hand, only around T_{comp}, two field-induced transitions are observed [Fig. 1(c)], which makes this compound exceptional in the RFe_5Al_7 family with heavy rare-earth metal.

At 26 and 34 K, the Er $4f$ and Fe $3d$ moments respond simultaneously to the magnetic field. At 26 K and H_{c1}, the Fe $3d$ moments align along the easy axis, causing the Er $4f$

moments to move toward [1$\bar{1}$0] to enlarge the angle between the two moments, while at 34 K and H_{c1}, the Er 4f moments align along the hard axis, causing the Fe 3d moments to move toward [1$\bar{1}$0] enlarging the angle between the two moments. At H_{c2}, the Er 4f and Fe 3d moments order at both temperatures with the transverse components almost compensated [see lower panels in Fig. 3(m)]. These observations indicate a significant contribution of the Er-Fe antiferromagnetic exchange interaction only around T_{comp}, where the sublattice moments have nearly the same magnitude with opposite sign.

Finally, we note a possible correlation between the hysteresis observed in the macroscopic results at the field-induced transitions below T_{comp} and the microscopic magnetic properties clarified by our soft XMCD results. In the magnetostriction results, above T_{comp}, there is negligible hysteresis, while below T_{comp}, the hysteresis becomes larger with decreasing temperature at the transitions [Fig. 1(b)]. Our XMCD results show that at H_{c1} below T_{comp} the Fe-moment rotate between the easy axes, while above T_{comp} the Er moments rotate between the easy and hard axis [Fig. 3(m)]. Therefore, the energetically unfavorable state with the moments along the hard axis lead to transitions with negligible hysteresis.

VI. ROTATION OF THE Er 4f MAGNETIC MOMENTS

In some R-T ferrimagnetic intermetallic systems, a field-induced transition from an initial collinear ferrimagnetic state directly to a forced-ferromagnetic state is suggested to be caused by longitudinal moment variations, namely by continuous demagnetization and remagnetization processes [8]. Here, noncollinear magnetic structures, caused by coherent magnetization rotations are not considered. These two mechanisms (coherent rotation vs continuous de/remagnetization) at field-induced transitions are difficult to be distinguished by bulk magnetization measurements which only probe longitudinal magnetization components.

In order to clarify whether the variations of the XMCD amplitudes in magnetic fields come from coherent moment rotations, which we assumed in the discussion above, we studied the field-dependent spectral lineshapes of the averaged XAS spectra [$= (\mu^+ + \mu^-)/2$]. Because light is inherently a transverse wave, the polarization-averaged XAS spectra are sensitive to linear dichroism (LD) resulting from variations in the magnetic-moment components perpendicular to the polarization plane. In other words, if coherent moment rotations occur and the ratio of the longitudinal to the transverse magnetic moment changes, there should be field-dependent changes in the spectral lineshapes of the averaged XAS [15].

Here, the longitudinal and transversal axes are parallel to the [110] and [$\bar{1}$10] axis, respectively. The [001] direction is also a transversal axis. However, the rotation of the Er moments from the basal plane toward the [001] axis is ignored because the [001] axis is the hardest axis. Since the LD is, in general, larger at the rare-earth M_5 edge than at the 3d transition-metal L edge, due to the larger spin-orbit coupling of the 4f orbitals, we investigated the field-dependent averaged XAS spectral lineshapes of the Er M_5 edge.

Figure 4(a) shows the averaged XAS spectra at selected magnetic fields at 34 K. There are three peak components at ~1403, 1405, and 1408 eV at the Er M_5 edge, which is

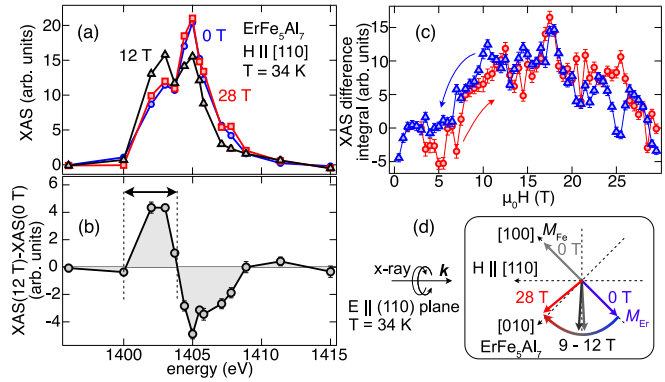

FIG. 4. (a) Er M_5-edge XAS spectra at 34 K at selected magnetic fields applied along the [110] axis. The spectra were obtained by the averaged sum of right- and left-circular polarized light. (b) XAS spectra at 0 T subtracted from the XAS spectra at 12 T at 34 K. (c) Magnetic-field dependence of the Er M_5-edge XAS difference signals obtained by integrating the range delimited by the two dashed lines in panel (b). (d) Direction of the Er 4f moment at selected magnetic fields with respect to the incoming beam with the propagation vector **k** and the principal crystallographic axes within the basal plane of $ErFe_5Al_7$. The electric field (E) of the x-ray beam is in the (110) plane.

a typical feature of Er^{3+} [28]. The spectral shape at 0 T is similar to that at 28 T, with a larger intensity at ~1405 eV and a smaller at ~1403 eV. At the intermediate magnetic field at 12 T, the spectral lineshape is clearly different. Here, the two peaks at 1403 and 1405 eV have almost the same amplitude. The high-energy peak at 1408 eV has a larger intensity at 0 and 28 T than at 12 T.

Figure 4(b) shows the XAS difference spectrum between the averaged XAS at 12 and 0 T. The spectral lineshape is similar to an x-ray linear dichroism spectrum typically obtained from polarization-dependent XAS using linear polarization [29]. Since the Er M_5-edge XMCD amplitude is almost zero at 12 T [Fig. 3(g)] right above the field-induced transition, the spectral contrast seen in comparison to the XAS at 0 T signals the change of the transversal component of the Er 4f moments in magnetic field. The integrated intensity of the positive peak between 1400 and 1404 eV in the Er M_5-edge XAS difference spectra is shown as a function of magnetic field in Fig. 4(c). The integrated intensity starts to increase at ~7 T with increasing magnetic field, reaches a maximum at intermediate magnetic field, and decreases at high magnetic fields toward 30 T, which corresponds to the rotation of the Er 4f moment schematically drawn in Fig. 4(d). At H_{c1}, the Er 4f moment is close to parallel to [$\bar{1}$10], which is perpendicular to the beam-propagation direction. These XAS data evidence the coherent moment rotation of the sublattice moments in $ErFe_5Al_7$.

VII. ROLE OF THE Er 5d MOMENTS

In R-T intermetallic compounds, R 5d electrons play an important role in the magnetic coupling between the R 4f and T 3d moments [3]. The microscopic behavior of the R 5d moments can be accessed via the electric-dipole transition

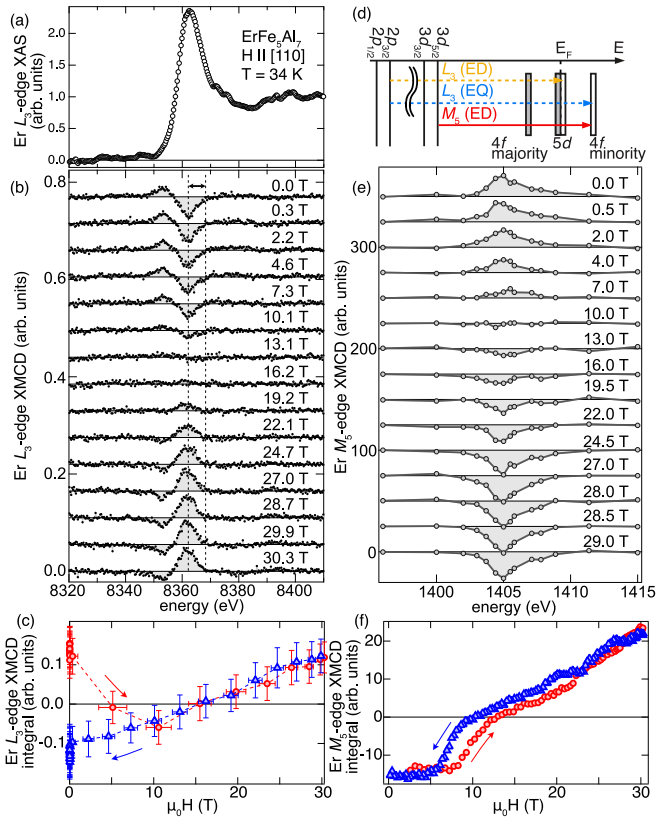

FIG. 5. (a) Er L_3-edge XAS spectra at 30.3 T. (b) Er L_3-edge XMCD spectra at selected magnetic fields. (c) Magnetic-field dependence of the XMCD signals obtained by integrating the range delimited by the two dashed lines in panel (b), where the electric-dipole transition ($2p_{3/2} \rightarrow 5d$) is predominantly involved. The lines are guides to the eye. (d) Schematic of the electronic structure involved in the electric-dipole (ED) and electric quadrupole (EQ) transitions at the Er L_3 and M_5 edges. (e) Er M_5-edge XMCD spectra at selected magnetic fields. (f) Er M_5-edge XMCD integrals as a function of magnetic field. The sign of the integrated XMCD signal is reversed as in Figs. 3(e)–3(l). The spectra in panels (b) and (e) were obtained during the down sweeps, respectively. Red and blue symbols in panels (c) and (f) are data from up and down sweep of magnetic fields. All results were measured at 34 K and for magnetic fields applied along the [110] axis.

($2p \rightarrow 5d$) in R L-edge XMCD experiments. Figure 5 shows a comparison of the XMCD results at the Er L_3 and M_5 edges at 34 K that allows us to study the shell-selective magnetic properties at the Er site across the field-induced transitions. The L_3-edge XMCD signal in the electric-dipole regime contains information on the $5d$ magnetic moments, while the M_5-edge XMCD directly probes the $4f$ moments.

Figure 5(a) shows a representative averaged XAS [$= (\mu^+ + \mu^-)/2$] spectrum, normalized by the edge jump, at 30.3 T applied along the [110] axis at 34 K. There is no detectable field dependence in the XAS spectra. Figures 5(b) and 5(e) show the Er L_3- and M_5-edge XMCD spectra at selected magnetic fields obtained during down sweeps, respectively. Both at the L_3 and M_5 edges, the XMCD amplitudes change with increasing magnetic fields. An analysis by singular value decomposition [30] of the L_3-edge XMCD shows that the present dataset is dominated by a single spectral component. This means that a possible contribution from the Fe sublattice transferred through the $3d$–$5d$ interaction is either absent or does not vary across this dataset (see Appendix C). In the following, we assume that the Er L_3-edge XMCD signal arises solely from the Er sublattice magnetization.

The Er L_3-edge XMCD spectra are composed of a pre-edge peak at 8353 eV and a main peak at ~8362 eV. The pre-edge peak of the Er L_3-edge XMCD spectra primarily originates from an electric-quadrupole (EQ) transition from $2p_{3/2}$ to empty $4f$ orbitals, while the main peak mainly comes from the electric-dipole (ED) transition from $2p_{3/2}$ to empty $5d$ orbitals [31] [Fig. 5(d)]. Earlier resonant (in)elastic x-ray scattering experiments [31,32] and theoretical calculations [33,34] show that the latter half of the main peak in R L-edge XMCD spectra predominantly comes from the ED transition that has an angular dependence of $\cos\theta$ (θ is the angle between the x-ray propagation vector and the $5d$ moments) [35–37].

In the current study of the Er L_3-edge XMCD spectra, this energy range is between 8362 eV and 8369 eV [see the two dashed lines in Fig. 5(b)]. Figure 5(c) shows the Er L_3-edge XMCD intensities integrated in the latter half of the main peak as a function of magnetic fields. This provides the relative variation of the $5d$ magnetic moments in magnetic fields. The $5d$ contribution to the bulk magnetization is, in general, smaller by, at least, one order of magnitude than the $4f$ electrons [38,39]. However, the overall feature of the variation of the Er $5d$ moments [Fig. 5(c)] follows that of the Er $4f$ moments [Fig. 5(f)]. This similarity elucidates the $4f$-$5d$ intra-atomic exchange coupling across the field-induced magnetic transitions.

The hysteresis below 5 T seen in the Er L_3-edge data is due to the different experimental procedure from that of the Er M_5-edge data. The Er L_3-edge XMCD spectra were obtained from data collected during two magnetic-field pulses with opposite field direction, while the Er M_5-edge XMCD spectra were extracted from two opposite circular polarizations using a fixed magnetic-field direction (see Appendix A).

VIII. THE TWO-SUBLATTICE MODEL

The high-field magnetization process has been analyzed by a two-sublattice model [4,40]. This simple model works for the RFe$_5$Al$_7$ systems with easy-plane (R = Tb [15] and Ho [13]) and easy-axis (R = Tm [14]) anisotropy when the magnetic fields are applied along an easy axis. Here, we apply this model for our high-field data under magnetic fields applied along the basal-plane hard axis. The model uses the following thermodynamic potential:

$$E(\alpha, \beta, H) = n_{\mathrm{ErFe}} M_{\mathrm{Er}} M_{\mathrm{Fe}} \cos(\alpha + \beta) + K\cos(4\beta) - \mu_0 H[M_{\mathrm{Fe}}\cos(\alpha) + M_{\mathrm{Er}}\cos(\beta)], \quad (1)$$

where the first, second, and third term are the intersublattice Er-Fe exchange interaction, magnetocrystalline anisotropy, and Zeeman energy. $n_{\mathrm{ErFe}} = 3.3$ T/μ_B [27] and K are the intersublattice exchange constant and the anisotropy constant in the basal plane, respectively. M_{Er} and M_{Fe} are the Er and Fe magnetic moments, respectively. α is the angle between M_{Fe} and the applied magnetic field and β is the angle between

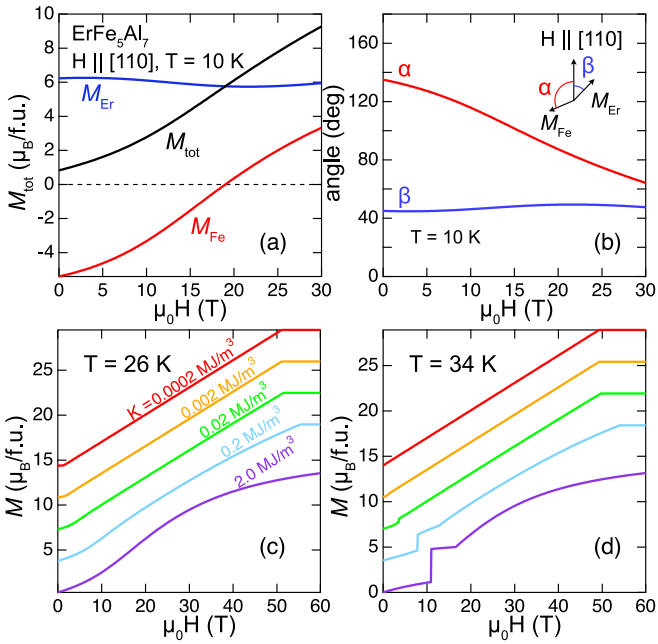

FIG. 6. (a) Field dependence of the Er (M_{Er}), Fe (M_{Fe}), and total magnetization (M_{tot}) at 10 K simulated by the two-sublattice model. (b) Field-dependent angles α and β defined with respect to the magnetic field (see inset). M_{tot} as a function of magnetic fields simulated for the selected anisotropy constants at (c) 26 K and (d) 34 K. The simulated results for different K are vertically shifted for clarity.

M_{Er} and the magnetic field [see inset of Fig. 6(b)]. $K > 0$ corresponds to the orientation of the magnetic field along the hard [110] axis. $K < 0$ is the case for magnetic fields applied along the easy [100] axis within the tetragonal basal plane.

We minimized the potential with respect to the angles α and β for a given magnetic field. We approximated M_{Fe} using the simple ferromagnetic compound $LuFe_6Al_6$ [41,42]. $LuFe_5Al_7$ does not suit this role as it displays an antiferromagnetic order at low temperatures that changes to ferromagnetic order at higher temperatures. First, we normalized M at 2 K of $LuFe_6Al_6$ to M_{Fe} [$= M_{\mathrm{s}}$–M_{Er} where M_{s} and M_{Er} are the spontaneous magnetization and Er^{3+} ground state value ($9\,\mu_{\mathrm{B}}$), respectively] at 2 K of $ErFe_5Al_7$ and $T_C = 327$ K of $LuFe_6Al_6$ to $T_{\mathrm{C}} = 201$ K of $ErFe_5Al_7$. Second, we subtracted the spontaneous magnetic moment from M_{Fe} to obtain M_{Er}.

In Figs. 6(a) and 6(b), the field dependencies of the Er $4f$ and Fe $3d$ moments as well as the angles α and β, respectively, are simulated using this model for the bulk magnetization and XMCD data [Figs. 3(a), 3(e), and 3(i)] at 10 K. The experimental data are well reproduced by this model with the anisotropy constant $K \sim 0.8$ MJ/m^3 at 10 K. The sign change of the Fe L_3-edge XMCD amplitude at ~18 T is well resolved in the simulation results. We note that using the same magnitude of K with opposite sign, $K \sim -0.8$ MJ/m^3, this model as well reproduces the magnetization process with two field-induced transitions experimentally observed [27] under magnetic fields applied along the [100] axis (not shown), which gives the reliability of the estimated K value at 10 K.

Figure 6(c) shows the change of the magnetization with respect to variations of K at 26 K. For $K = 0.0002$ MJ/m^3, there is a kink at ~1.5 T above which the magnetization increases monotonously up to 50 T, where the magnetization saturates. With increasing K, the low-field kink smears out and the magnetization grows without any features up to saturation. Figure 6(d) shows the evolution of the magnetization at 34 K at the same K as those in Fig. 6(c). Up to $K = 0.002$ MJ/m^3, the magnetization gradually increases until it saturates. For $K = 0.02$–2.0 MJ/m^3, magnetization jumps appear in the field range between 3.5 T and 11 T. At both temperatures, 26 K and 34 K, for K larger than 2.0 MJ/m^3, there are no qualitative changes of the magnetization curves. The experimental results with two field-induced transitions under magnetic fields along the basal-plane hard axis [Figs. 3(b) and 3(c)] are not reproduced within this model. This agrees with earlier theoretical studies [43] that two phase transitions cannot be predicted by the two-sublattice model for magnetic fields applied along the basal-plane hard axis.

A refined model is required for a more detailed description of the high-field magnetization processes around T_{comp} where the two field-induced transitions appear. It is interesting how the Er $4f$ moments rotate from the easy to the hard axis at H_{c1} by overcoming the magnetocrystalline anisotropy. Contributions from magnetoelastic interactions are not considered in our model. Our magnetostriction results give the relative lattice change along the [110] axis. However, the volume variations in magnetic fields are still not known. Local crystal distortions or symmetry changes in magnetic fields might influence the magnetic properties around T_{comp}. In addition, noncollinear magnetic structures below some temperature close to T_{comp} cannot be excluded, which calls for detailed elastic neutron-scattering studies. Such a magnetic symmetry reduction around T_{comp} has been reported in rare-earth iron garnets [44,45]. A crystal-field level scheme, as well, could help modeling the magnetic properties under magnetic field. In our model, we consider the magnetocrystalline anisotropy using the macroscopic basal-plane anisotropy constant K. In this respect, inelastic neutron scattering measurements would be needed to determine the crystal-field energy levels. Microscopic modeling can explain the high-field magnetic properties around T_{comp} by taking into account exchange interactions between individual atoms, such as the Fe atoms in the $8f$ and $8j$ positions and the Er atoms, and possible slight changes in the band structure in magnetic fields, in addition to the magnetostriction, crystal-field effects, and possible noncollinear magnetic structures.

IX. CONCLUSIONS

We presented advanced high-field x-ray spectroscopy results of the highly anisotropic ferrimagnet $ErFe_5Al_7$, focusing on the microscopic analysis of the reorientation of the element-specific magnetic moments at the two field-induced magnetic transitions around T_{comp} for fields applied along the hard magnetization axis [110]. In particular, we found that at 34 K, close to the compensation temperature, the low-field magnetic transition at H_{c1} originates from the rotation of the Er $4f$ magnetic moments from the easy to the hard axis. In addition, the Er $5d$ moments follow the rotation of the Er $4f$ moments due to the intra-atomic $4f$-$5d$ exchange coupling across the field-induced transitions. We evaluated a magnetocrystalline anisotropy constant by simulating the

magnetization process at 10 K using a two-sublattice model. Further refinement of the model is required to describe the complex element-specific magnetization processes with field-induced magnetic transitions around the compensation point.

ACKNOWLEDGMENTS

We would like to thank N. V. Kostyuchenko, N. V. Mushnikov, and Y. Skourski for fruitful discussions. We acknowledge support from the Deutsche Forschungsgemeinschaft (DFG) through SFB 1143 (Project No. 247310070), the Würzburg-Dresden Cluster of Excellence on Complexity and Topology in Quantum Matter–*ct.qmat* (EXC 2147, Project No. 390858490), and the Czech Science Foundation (Project No. 21-09766S). Crystal growth and partial sample preparation were performed at MGML [46] within the Program of Czech Research Infrastructures (Projects No. LM2018096 and No. LM 2023065), as well as the support of the HLD at HZDR, member of the European Magnetic Field Laboratory (EMFL). The pulsed-field x-ray experiments were performed on beamline ID24 at the European Synchrotron Radiation Facility (ESRF), Grenoble, France (Proposal No. HC-3785) and at the UE46-PGM1 undulator beamline of BESSY II (under GIMRT/ICC-IMR collaboration).

APPENDIX A: PULSED-FIELD X-RAY MAGNETIC DICHROIC EXPERIMENTS

Figure 7 shows the time dependence of the magnetic-field pulses used in the Er M- and Fe L-edge experiments at the UE46-PGM1 at BESSY II and Er L_3-edge experiments at ID24 of ESRF. A charging voltage of 1.5 kV with a capacitance of 6.4 mF was used for the 30-T field pulses at BESSY II. A charging voltage of 8 kV with a capacitance of 4 mF [47] was used for the 30-T field pulses at ESRF.

At BESSY II, the field-dependent TEY signals were measured with a sampling rate of 31.25 MHz and with a bandwidth of a current amplifier of 20 kHz for the amplification rate of 10^{10} V/A and of 30 kHz for 10^9 V/A for the sample TEY current. To obtain a clean surface, the sample was cleaved *in situ* parallel to the (110) plane, which is

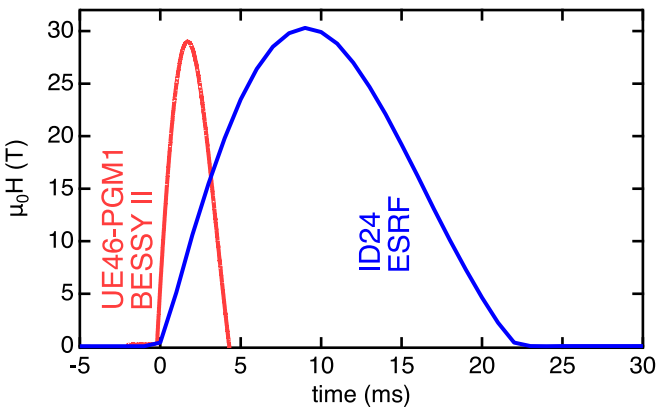

FIG. 7. Time dependence of the pulsed magnetic field used for soft (red) and hard (blue) x-ray dichroic measurements at UE46-PGM1 BESSY II and ID24 ESRF, respectively.

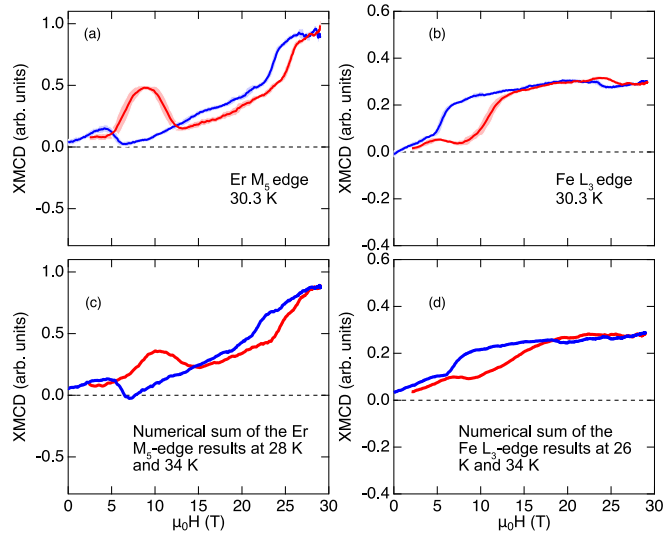

FIG. 8. Field-dependent XMCD amplitude at 30.3 K at the (a) Er M_5 edge and (b) at the Fe L_3 edge. Numerical sum of the field-dependent XMCD amplitudes (c) at the Er M_5 edge at 28 and 34 K and (d) at the Fe L_3 edge at 26 and 34 K. Red and blue lines are data from up and down field sweeps

normal to the beam-propagation direction, at pressures below 1×10^{-9} mbar at BESSY II. The Er M_5-edge XAS and XMCD spectra were obtained by measuring the TEY signals at each energy point for both plus (μ^+) and minus (μ^-) light helicities. Magnetic-field pulses with a maximum of 30 T were used for all soft x-ray dichroic measurements.

At the energy-dispersive x-ray absorption beamline ID24 [23] at the ESRF, the Er L_3-edge XMCD data were recorded using a multiframe acquisition scheme [48]. The sample was oriented along the [110] axis, cut, and mechanically polished to a thin platelet. The thickness was ∼16 μm. This sample piece was sandwiched between two diamond windows, which was mounted in a He-flow cryostat, where the sample was cooled by forced convection. The Er L_3-edge spectra were obtained in a way that all the energy points were recorded simultaneously during a single magnetic-field pulse. To improve the statistics, results for 92 magnetic-field pulses were averaged for the Er L_3-edge spectra [Figs. 5(a)–5(c)]. Positive (+30 T) and negative (–30 T) field pulses were alternately generated under a fixed circular polarity and the transmission intensity was measured. This pulse sequence results in the hysteresis at low magnetic fields shown in Fig. 5(c).

APPENDIX B: MAGNETIC DOMAINS AROUND T_{COMP}

Figures 8(a) and 8(b) show the Er M_5-edge and Fe L_3-edge XMCD amplitudes as a function of magnetic fields at 30.3 K, respectively. Figure 8(c) displays the numerical sum of the field-dependent Er M_5-edge XMCD amplitudes at 28 K (data not shown) and 34 K [Fig. 3(g)]. Figure 8(d) displays the numerical sum of the field-dependent Fe L_3-edge XMCD amplitudes at 26 K [Fig. 3(j)] and 34 K [Fig. 3(k)]. The numerical sums show similar field dependencies to those observed at 30.3 K. This means that at 30.3 K, some areas have magnetic domains with the Er $4f$ moments pointing along [100] and

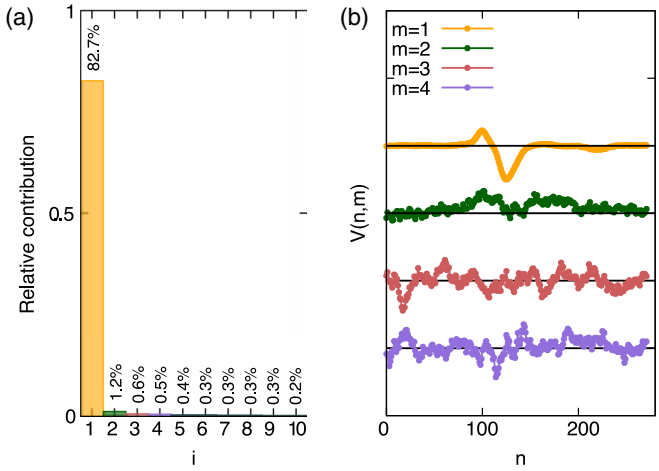

FIG. 9. SVD analysis for the Er L_3-edge XMCD spectral data. (a) Contribution of components to the variance of dataset [Fig. 5(b)]. (b) First four components.

with the Fe 3*d* moments along [$\bar{1}$00], and others have domains with opposite direction of the Er 4*f* and Fe 3*d* moments. The former domain is characterized by a decrease of the Er XMCD amplitudes [Fig. 3(f)] and an increase of the Fe XMCD amplitudes [Fig. 3(j)] at H_{c1}. The latter domain is characterized by an increase of the Er XMCD amplitudes [Fig. 3(g)] and a decrease of the Fe XMCD amplitudes [Fig. 3(k)] at H_{c1}. Here, we assume that at 26 and 28 K, almost 100% of the probed volume contains the former domain, and at 34 K it contains the latter domain. This analysis points to the existence of magnetic domains around T_{comp}.

APPENDIX C: SINGULAR-VALUE-DECOMPOSITION ANALYSIS FOR THE Er L_3-EDGE XMCD SPECTRA

In *R*-*T* systems, sizable *R* (*T*) contributions can appear in *T* *K*-edge (*R* *L*-edge) XMCD spectra as shown for garnet oxides and intermetallic compounds [49,50]. Recently, such mixed contributions were mathematically decomposed by a singular-value-decomposition (SVD) analysis [30]. We performed such an analysis for our Er L_3-edge XMCD spectral data [Fig. 5(b)]. Figure 9(a) shows the specific gravity of the first 10 components. The first four components corresponds to the spectral lineshapes shown in Fig. 9(b). The SVD analysis indicates that the dataset is dominated by a single component. The first component accounts for 82.7% of the variance of the dataset. The second and higher components contain negligible spectral information within the available statistics. A contribution form the Fe sites is, thus, either strictly correlated with the Er signal or absent.

[1] R. Skomski and J. M. D. Coey, *Permanent Magnetism* (CRC Press, Boca Raton, FL, 1999).

[2] M. D. Kuz'min, Y. Skourski, D. Eckert, M. Richter, K.-H. Müller, K. P. Skokov, and I. S. Tereshina, Spin reorientation in high magnetic fields and the Co-Gd exchange field in $GdCo_5$, Phys. Rev. B **70**, 172412 (2004).

[3] I. A. Campbell, Indirect exchange for rare earths in metals, J. Phys. F: Met. Phys. **2**, L47 (1972).

[4] J. J. M. Franse and R. J. Radwański, Magnetic properties of binary rare-earth 3d-transition-metal intermetallic compounds, in *Handbook of Magnetic Materials*, Vol. 7, edited by K. H. J. Buschow (Elsevier, Amsterdam, 1993), p. 307.

[5] R. Ballou, B. Gorges, R. Lemaire, H. Rakoto, and J. C. Ousset, Field induced transition from collinear to canted magnetic structures in $TbCo_5$, Phys. B: Condens. Matter **155**, 266 (1989).

[6] J. J. M. Franse, F. E. Kayzel, and N. P. Thuy, Exchange and anisotropy in 3d-4f compounds, J. Magn. Magn. Mater. **129**, 26 (1994).

[7] H. Kato, D. W. Lim, M. Yamada, Y. Nakagawa, H. A. Katori, and T. Goto, Field-induced phase transitions in ferrimagnetic $R_2Fe_{14}B$ in ultra-high magnetic fields, Phys. B: Condens. Matter **211**, 105 (1995).

[8] A. V. Andreev, M. D. Kuz'min, Y. Narumi, Y. Skourski, N. V. Kudrevatykh, K. Kindo, F. R. de Boer, and J. Wosnitza, High-field magnetization study of a TM_2Co_{17} single crystal, Phys. Rev. B **81**, 134429 (2010).

[9] O. Isnard, A. V. Andreev, M. D. Kuz'min, Y. Skourski, D. I. Gorbunov, J. Wosnitza, N. V. Kudrevatykh, A. Iwasa, A. Kondo, A. Matsuo, and K. Kindo, High magnetic field study of the Tm_2Fe_{17} and $Tm_2Fe_{17}D_{3.2}$ compounds, Phys. Rev. B **88**, 174406 (2013).

[10] A. E. Clark, and E. Callen, Néel ferrimagnets in large magnetic fields, J. Appl. Phys. **39**, 5972 (1968).

[11] A. K. Zvezdin, Field induced phase transitions in ferrimagnets, in *Handbook of Magnetic Materials*, edited by K. H. J. Buschow, Vol. 9 (Elsevier, Amsterdam, 1995), p. 405.

[12] D. I. Gorbunov, S. Yasin, A. V. Andreev, Y. Skourski, N. V. Mushnikov, E. V. Rosenfeld, S. Zherlitsyn, and J. Wosnitza, Magnetic anisotropy and magnetic phase transitions in RFe_5Al_7, J. Magn. Magn. Mater. **383**, 208 (2015).

[13] D. I. Gorbunov, C. Strohm, M. S. Henriques, P. van der Linden, B. Pedersen, N. V. Mushnikov, E. V. Rosenfeld, V. Petříček, O. Mathon, J. Wosnitza, and A. V. Andreev, Microscopic nature of the first-order field-induced phase transition in the strongly anisotropic ferrimagnet $HoFe_5Al_7$, Phys. Rev. Lett. **122**, 127205 (2019).

[14] Sh. Yamamoto, D. I. Gorbunov, H. Akai, H. Yasumura, Y. Kotani, T. Nakamura, T. Kato, N. V. Mushnikov, A. V. Andreev, H. Nojiri, and J. Wosnitza, Element- and orbital-selective magnetic coherent rotation at the first-order phase transition of a hard uniaxial ferrimagnet, Phys. Rev. B **101**, 174430 (2020).

[15] Sh. Yamamoto, D. I. Gorbunov, I. F. Diaz-Ortega, A. Miyata, T. Kihara, Y. Kotani, T. Nakamura, N. V. Mushnikov, A. V. Andreev, H. Nojiri, and J. Wosnitza, High-field soft-x-ray dichroism of a hard ferrimagnet with easy-plane anisotropy, Phys. Rev. B **104**, 064405 (2021).

[16] W. Kockelmann, W. Schäfer, G. Will, P. Fischer, and J. Gal, Neutron diffraction study of the ferrimagnetic structures of RFe_5Al_7 compounds with R = Tb, Dy, Ho, Er, Tm, J. Alloys Compd. **207-208**, 311 (1994).

[17] D. I. Gorbunov, and A. V. Andreev, Magnetization study of single-crystalline $ErFe_5Al_7$, J. Alloys Compd. **556**, 109 (2013).

[18] Y. Skourski, M. D. Kuz'min, K. P. Skokov, A. V. Andreev, and J. Wosnitza, High-field magnetization of Ho_2Fe_{17}, Phys. Rev. B **83**, 214420 (2011).

[19] G. Asti, and F. Bolzoni, Theory of first order magnetization processes: Uniaxial anisotropy, J. Magn. Magn. Mater. **20**, 29 (1980).

[20] G. Asti, First-order magnetic processes, in *Handbook of Magnetic Materials*, Vol. **5**, edited by K. H. J. Buschow and E. P. Wohlfarth (Elsevier, Amsterdam, 1990), p. 397.

[21] R. Daou, F. Weickert, M. Nicklas, F. Steglich, A. Haase, and M. Doerr, High resolution magnetostriction measurements in pulsed magnetic fields using fiber Bragg gratings, Rev. Sci. Instrum. **81**, 033909 (2010).

[22] P. Frings, J. Vanacken, C. Detlefs, F. Duc, J. E. Lorenzo, M. Nardone, J. Billette, A. Zitouni, W. Bras, and G. L. J. A. Rikken, Synchrotron x-ray powder diffraction studies in pulsed magnetic fields, Rev. Sci. Instrum. **77**, 063903 (2006).

[23] S. Pascarelli, O. Mathon, T. Mairs, I. Kantor, G. Agostini, C. Strohm, S. Pasternak, F. Perrin, G. Berruyer, P. Chappelet *et al.*, The Time-resolved and Extreme-conditions XAS (TEXAS) facility at the European Synchrotron Radiation Facility: The energy-dispersive x-ray absorption spectroscopy beamline ID24, J. Synchrotron Rad. **23**, 353 (2016).

[24] A. V. Andreev, Y. Skourski, M. D. Kuz'min, S. Yasin, S. Zherlitsyn, R. Daou, J. Wosnitza, A. Iwasa, A. Kondo, A. Matsuo, and K. Kindo, Magnetic and magnetoelastic anomalies of an Er_2Co_{17} single crystal in high magnetic fields, Phys. Rev. B **83**, 184422 (2011).

[25] F. Donati, A. Singha, S. Stepanow, C. Wäckerlin, J. Dreiser, P. Gambardella, S. Rusponi, and H. Brune, Magnetism of Ho and Er atoms on close-packed metal surfaces, Phys. Rev. Lett. **113**, 237201 (2014).

[26] C. T. Chen, Y. U. Idzerda, H.-J. Lin, N. V. Smith, G. Meigs, E. Chaban, G. H. Ho, E. Pellegrin, and F. Sette, Experimental confirmation of the x-ray magnetic circular dichroism sum rules for iron and cobalt, Phys. Rev. Lett. **75**, 152 (1995).

[27] D. I. Gorbunov, S. Yasin, A. V. Andreev, Y. Skourski, S. Zherlitsyn, and J. Wosnitza, Magnetization and magnetoacoustics of single-crystalline $ErFe_5Al_7$ in high magnetic fields, J. Magn. Magn. Mater. **357**, 61 (2014).

[28] J. B. Goedkoop, B. T. Thole, G. van der Laan, G. A. Sawatzky, F. M. F. de Groot, and J. C. Fuggle, Calculations of magnetic x-ray dichroism in the 3*d* absorption spectra of rare-earth compounds, Phys. Rev. B **37**, 2086 (1988).

[29] P. Castrucci, F. Yubero, F. C. Vicentin, J. Vogel, and M. Sacchi, Surface crystal field at the Er/Si(111) interface studied by soft-x-ray linear dichroism, Phys. Rev. B **52**, 14035 (1995).

[30] C. Strohm, P. van der Linden, O. Mathon, and S. Pascarelli, Simultaneous observation of the Er- and Fe-sublattice magnetization of ferrimagnetic $Er_3Fe_5O_{12}$ in high magnetic fields using x-ray magnetic circular dichroism at the Er $L_{2,3}$ edges, Phys. Rev. Lett. **122**, 127204 (2019).

[31] F. Bartolomé, J. M. Tonnerre, L. Seve, D. Raoux, J. Chaboy, L. M. Garcia, M. Krisch, and C. C. Kao, Identification of quadrupolar excitation channels at the L_3 edge of rare-earth compounds, Phys. Rev. Lett. **79**, 3775 (1997).

[32] L. Bouchenoire, A. Mirone, S. D. Brown, P. Strange, T. Wood, P. Thompson, D. Fort, and J. Fernández-Rodríguez, E1 and E2 contributions to the L_3 resonance line shape in antiferromagnetic holmium, New J. Phys. **11**, 123011 (2009).

[33] J. C. Parlebas, K. Asakura, A. Fujiwara, I. Harada, and A. Kotani, X-ray magnetic circular dichroism at rare-earth L_{23} absorption edges in various compounds and alloys, Phys. Rep. **431**, 1 (2006).

[34] H. Wende, Z. Li, A. Scherz, G. Ceballos, K. Baberschke, A. Ankudinov, J. J. Rehr, F. Wilhelm, A. Rogalev, D. L. Schlagel, and T. A. Lograsso, Quadrupolar and dipolar contributions to x-ray magnetic circular dichroism at the Tb $L_{3,2}$ edges: Experiment versus theory, J. Appl. Phys. **91**, 7361 (2002).

[35] P. Carra, and M. Altarelli, Dichroism in the x-ray absorption spectra of magnetically ordered systems, Phys. Rev. Lett. **64**, 1286 (1990).

[36] J. C. Lang, G. Srajer, C. Detlefs, A. I. Goldman, H. König, X. Wang, B. N. Harmon, and R. W. McCallum, Confirmation of quadrupolar transitions in circular magnetic x-ray dichroism at the Dysprosium L_{III} edge, Phys. Rev. Lett. **74**, 4935 (1995).

[37] J. Chaboy, F. Bartolomé, L. M. García, and G. Cibin, Evidence of quadrupolar transitions in the circular dichroism at the neodymium L_2 and L_3 edges, Phys. Rev. B **57**, R5598 (1998).

[38] W. C. Koehler, Magnetic properties of rare-earth metals and alloys, J. Appl. Phys. **36**, 1078 (1965).

[39] E. Burzo, L. Chioncel, R. Tetean, and O. Isnard, On the R 5d band polarization in rare-earth–transition metal compounds, J. Phys.: Condens. Matter **23**, 026001 (2010).

[40] M. D. Kuz'min, High-field low-temperature magnetisation curves of anisotropic ferrimagnets, J. Magn. Magn. Mater. **323**, 1068 (2011).

[41] D. I. Gorbunov, A. V. Andreev, S. Daniš, and J. Pospíšil, Evolution of magnetism in $LuFe_xAl_{12-x}$ ($4 \leqslant x \leqslant 6$) single crystals, J. Alloys Compd. **563**, 63 (2013).

[42] A. V. Andreev, Magnetic anisotropy of UFe_6Al_6, Phys. B: Condens. Matter **404**, 2978 (2009).

[43] D. I. Gorbunov, A. V. Andreev, Y. Skourski, and M. D. Kuz'min, High-field magnetization of a $DyFe_5Al_7$ single crystal, J. Alloys Compd. **553**, 358 (2013).

[44] R. Hock, H. Fuess, T. Vogt, and M. Bonnet, Low temperature magnetic structure of erbium iron garnet, Z. Phys. B **82**, 283 (1991).

[45] M. Guillot, F. Tchéou, A. Marchand, and P. Feldmann, Temperature evolution of the umbrella structure in holmium iron garnet, Z. Phys. B **56**, 29 (1984).

[46] https://mgml.eu.

[47] F. Duc, X. Fabrèges, T. Roth, C. Detlefs, P. Frings, M. Nardone, J. Billette, M. Lesourd, L. Zhang, A. Zitouni, *et al.*, A 31 T split-pair pulsed magnet for single crystal x-ray diffraction at low temperature, Rev. Sci. Instrum. **85**, 053905 (2014).

[48] C. Strohm, F. Perrin, M.-C. Dominguez, J. Headspith, P. van der Linden, and O. Mathon, Multi-frame acquisition scheme for efficient energy-dispersive X-ray magnetic circular dichroism in pulsed high magnetic fields at the Fe *K*-edge, J. Synchrotron Rad. **18**, 224 (2011).

[49] N. Kawamura, M. Suzuki, H. Maruyama, and T. Ishikawa, Variation of XMCD spectrum with temperature at R $L_{2,3}$-edges in $R_3Fe_5O_{12}$ (R= Gd and Er), J. Synchrotron Radiat. **8**, 425 (2001).

[50] R. Boada, C. Piquer, M. A. Laguna-Marco, and J. Chaboy, Additivity of magnetic contributions to the x-ray magnetic circular dichroism spectrum, Phys. Rev. B **81**, 100404(R) (2010).